Available online at www.sciencedirect.com
ScienceDirect
Journal of Power Sources 172 (2007) 542–552
JOURNAL OF POWER SOURCES
www.elsevier.com/locate/jpowsour

An investigation of water-gas transport processes in the gas-diffusion-layer of a PEM fuel cell by a multiphase multiple-relaxation-time lattice Boltzmann model

Xiao-Dong Niu [a,*], Toshihisa Munekata [a], Shi-Aki Hyodo [a], Kazuhiko Suga [b]

[a] *Computational Physics Lab., Toyota Central R&D Labs., Inc., Nagakute, Aichi 480-1192, Japan*
[b] *Department of Mechanical Engineering, Osaka Prefecture University, Sakai 599-8531, Japan*

Received 5 February 2007; received in revised form 8 May 2007; accepted 21 May 2007
Available online 25 May 2007

Abstract

In order to study water-gas transport processes in the gas-diffusion-layer (GDL) of a proton exchange membrane (PEM) fuel cell system, a multiphase, multiple-relaxation-time lattice Boltzmann model is presented in this work. The model is based on the mean-field diffuse interface theory and can handle the multiphase flows with large density ratios and various viscosities. By using the standard bounce back boundary condition and an approximate average scheme for the non-slip and wetting boundary walls, respectively, detailed liquid-gas transportation in the GDL, in which exact boundary condition is difficult to be implemented, can be simulated. Unlike most of lattice Boltzmann methods based on the Bhatnagar–Gross–Krook collision operator, the present model shows a viscosity-independent velocity field, which is very important in simulating multiphase flows where various viscosities coexist. We validate our model by simulating a static droplet on a wetting wall and compare with theoretical predictions. Then, we simulate a water-gas flow in the GDL of a PEM fuel cell and investigate the saturation-dependent transport properties under different conditions. The results are shown to be qualitatively consistent with the previous numerical and theoretical works.

Keywords: Multiphase flows; Lattice Boltzmann model; Transport properties; Gas-diffusion-layer; Fuel cell

1. Introduction

The proton exchange membrane (PEM) fuel cell is considered as one of the best approaches in the search of new energy sources. In the PEM fuel cell, two reactant gases, hydrogen and oxygen, combine at a membrane of about 50 μm thickness covered with a catalytic layer. The membrane is surrounded by a gas-diffusion-layer (GDL) of about 200 μm thickness. In this setup, the GDL plays an important role because it has several specific functions such as providing a continuous transport of the reactant gases and electronic conductivity between anode and cathode [1]. However, since the PEM fuel cell is usually operated with humidified reactant gases at lower temperatures, a so-called "flooding" phenomenon, particularly on the cathode side where the water vapors condense and block the pores of the GDL, is possibly caused and hence degenerates the performance of the fuel cell. Therefore, it is vital to investigate the liquid-gas transport in the GDL and study the transport properties so that the diffusion media with optimal performance can be found.

In the literature, to simulate liquid-gas two-phase flows in the GDL, Darcy's law is usually applied for both phases with properties especially for two-phase effects. The properties are capillary pressure, which is the pressure difference between two phases, and relative permeability, which adjust the permeability of the Darcy's law for each phase. These properties can be functions of liquid saturation, which is ratio of liquid volume to pore volume. Since the GDL is usually a complex random microstructure, it is very difficult to characterize its exact geometry and so to calculate the transport properties [2]. Such difficulties can be illustrated in Fig. 1, which shows a micrograph of the Toray TGP-H-60 as a typical example and visualizations of the reconstructed three-dimensional (3D) geometries via the virtual material design and the dissipative particle dynamics (DPD), respectively. Obviously, one can clearly see the strong anisotropy of the medium structure.

* Corresponding author. Tel.: +81 561 71 7111; fax: +81 561 63 5258.
E-mail address: e1351@mosk.tytlabs.co.jp (X.-D. Niu).

0378-7753/$ – see front matter © 2007 Elsevier B.V. All rights reserved.
doi:10.1016/j.jpowsour.2007.05.081

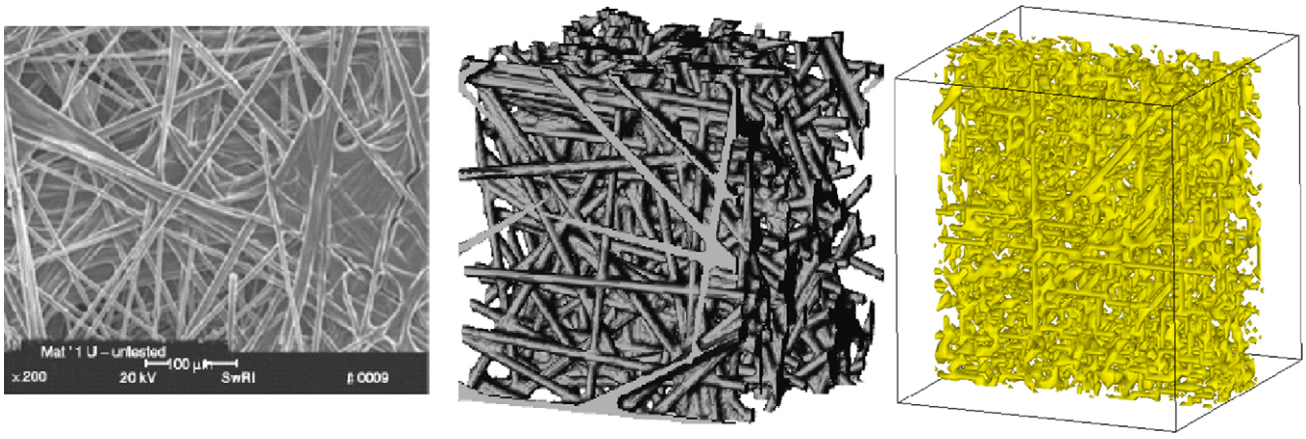

Fig. 1. Micrograph of the Toray TGP-H-60 and visualizations of reconstructed 3D-geometries generated by the virtual material design (middle) and the dissipative particle dynamics (right), respectively.

Conventionally, to elucidate the two-phase transport phenomena in the GDL, various numerical models have been developed. The simplest approach is a single-phase model, in which gas and liquid are considered as a single-fluid mixture and thus share the same velocity field. Also, the interfacial tension effect is completely ignored. In this case, the total amount of water can be obtained by solving a single equation without distinguishing water vapor from liquid water. Once the total water concentration field is obtained, one may allow for the water concentration going beyond the saturation level, essentially assuming super saturation in the gas phase [3–5]. The more rigorous approach to liquid water transportation in the GDL is a reformulation model in which the classical two-phase models is reformulated into a single equation, and the interfacial tension effect and GDL wettability, essential for successful fuel cell operation, are fully accounted for [6–10]. This model can efficiently produce most of the GDL characteristics, but neglect the local structure details. Another approach is in terms of volume-averaged or pore-level models [11–16]. These models assume local interfacial equilibrium, namely, electrical, chemical, and thermal equilibrium at the pore level. Conditions of validity of local interfacial equilibrium were carefully defined. All of the above-cited models are, strictly speaking, macroscopic models, although theoretical inconsistency may exist in some works, and by nature any interface boundary between two fluid phases is mesoscopic. Therefore, it is desirable to develop a mesoscopic model to study the two-fluid flows.

Recently, as a mesoscopic model, the lattice Boltzmann (LB) method has become a promising tool to simulate the multiphase flows [17–23]. The LB method originated from the lattice gas cellular automata (LGCA) [24,25]. Due to its kinetic origin, the LB method poses some features that are different from the macroscopic models. These features include programming simplicity, intrinsic parallelism and straightforward resolution of complex boundaries and multiple fluid species. The later two features are quite appealing in simulating multiphase flows in the GDL-like structures. In these cases, the fluid–solid interface is approximated by a zigzag approach so that the standard bounce back boundary condition can be directly applied, which reverse the momentum of fluid particles colliding with a solid boundary by mimicking the particle–solid interaction for non-slip boundary condition. However, the majority of the LB methods used in modeling multiphase flows are based on the Bhatnagar–Gross–Krook (BGK) collision model [26,27] and they often encounter problems such as numerical instabilities and viscosity-dependent velocity field [23,28]. Since various viscosities are usually presented simultaneously in the two-phase flows, the above limits become critical in accuracy of numerical simulations. To overcome these drawbacks, a multiple-relaxation-time (MRT) LB model is developed [22,23,28]. It has been demonstrated that the MRTLB model has better stability and accuracy in simulating the multiphase flows than the BGK counterparts [22,23]. However, most of the MRT multiphase models are based on the single-component potential model [18], which mimic two-phase flows by adjusting the interaction potentials and can only be effective for two-phase flows with small density ratios ($\leq$100). A two-distribution-function MRTLB model was recently proposed and it overcomes most limits of the previous BGK and MRT model but requires an implicit treatment of the interface tension [29].

In this paper, a MRTLB model for multiphase flows with large density ratios and various viscosities is developed and applied to simulate water-gas transportations in the GDL of a PEM fuel cell. The model is based on the diffuse interface theory [30,31]. To handle the large density ratios and various viscosities, two distribution functions are employed in this model, and one of which is used for modeling velocity field with total density of different phases, and the other is for tracking the interface by including effects of density differences between different phases. Unlike the previous MRT models, in which the interface tension and wetting boundary condition must be calculated in advance based on the static droplet on the solid walls, the present model explicitly incorporates both factors. To catch the boundary effects, besides the standard bounce back condition used to mimic the non-slip boundary condition, an approximated average approach based on the Taylor series expansion is presented to model the wetting boundaries.

The rest of this paper is organized as follows. In Section 2, a multiphase MRTLB model is presented. We first give a brief introduction of the diffuse interface theory, and then present the

MRTLB equations followed by numerical implementations of the non-slip and wetting boundary conditions. Section 3 includes two parts. In the first part this model is validated by simulating a static droplet on a wetting wall and the results are compared with theoretical solutions. In the second part, numerical simulations of the liquid-gas flows in the tentative model of GDL are carried out and the transport properties are investigated. We close with a conclusion in Section 4.

2. Multiphase, multiple-relaxation-time lattice Boltzmann model

2.1. Diffuse interface theory

Our model is based on the diffuse interface theory [29,30]. Here, we consider a flow with two fluids or phases such as gas and liquid which have mass densities of ρ_g and ρ_l and viscosities of η_g and η_l, respectively. The whole flow system is characterized by the mass density $\rho = \rho_l + \rho_g$, the viscosity $\eta = \eta_l + \eta_g$ and the local order parameter φ denoting the density difference of two phases. The thermodynamic behavior of the system can then be described by the following free energy functional

$$F = \int \mathrm{d}V \left(\psi + \frac{k}{2} |\nabla \varphi|^2 \right) + \int \mathrm{d}S \, \psi_s, \tag{1}$$

where V is a control volume and S is the surface area of the wetting wall. The first integral on the right-hand side is the standard Ginzburg–Landau expression with a bulk free energy density ψ defined by [31]

$$\psi = A(\varphi^2 - 1)^2, \tag{2}$$

where the parameters k and A determine the interface tension $\sigma = 4\sqrt{2kA}/3$, and interface width $\xi = \sqrt{2k/A}$ [32]. With this form of the bulk free energy, the system will contribute to two equilibrium states, -1 and $+1$, corresponding low and high density fields, respectively.

The second term in Eq. (1) accounts for specific wetting interactions at the solid–fluid boundaries due to the surface energy ψ_s. Functional minimization of F requires

$$\psi_s = k\varphi(\mathbf{n} \cdot \nabla \varphi), \tag{3}$$

which is evaluated at the solid wall, where $\mathbf{n}$ is the surface normal pointing to fluids [33]. This condition leads to a static contact angle θ at a flat wall in the absence of flow such that the wetting potential γ has

$$\gamma = -k\mathbf{n} \cdot \nabla \varphi = 2\mathrm{sign}\left(\frac{\pi}{2} - \theta\right) \sqrt{\cos\frac{\beta}{3}\left(1 - \cos\frac{\beta}{3}\right)} \sqrt{2Ak}, \tag{4}$$

where $\beta = \arccos(\sin^2\theta)$. Given the free energy functional of Eq. (1), the dynamic behavior of the two-phase fluid is governed by the Navier–Stokes equations,

$$\frac{\partial \rho \mathbf{u}}{\partial t} + \nabla \cdot \rho \mathbf{u}\mathbf{u} = -\nabla \cdot \mathbf{P} + \eta \nabla^2 \mathbf{u} + \mathbf{F}_b, \tag{5}$$

and the Cahn–Hilliard equation,

$$\frac{\partial \varphi}{\partial t} + \nabla \cdot \varphi \mathbf{u} = M \nabla^2 \mu, \tag{6}$$

with $\mathbf{u}$ being the macroscopic fluid velocity, $\mathbf{F}_b$ the body force and M is the mobility. The gradient of the pressure tensor $\mathbf{P}$ and the chemical potential μ are written as [30–32]

$$\nabla \cdot \mathbf{P} = \nabla(\rho c_s^2 + \mu\varphi) - \mu \nabla \varphi, \tag{7}$$

and

$$\mu = \frac{\partial \psi}{\partial \varphi} - k\nabla^2 \varphi, \tag{8}$$

respectively, and c_s is the sound speed given later. The bulk pressure of the system can be calculated as

$$p = \rho c_s^2 + \varphi \frac{\partial \psi}{\partial \varphi} - \psi - k\left(\varphi \nabla^2 \varphi - \frac{1}{2}|\nabla \varphi|^2\right). \tag{9}$$

2.2. MRTLB method

In the framework of the MRT lattice Boltzmann method with N discrete velocities [28,29], Eqs. (5) and (6) can be solved by the following two equations:

$$\mathbf{f}(\mathbf{r} + \mathbf{e}_i \delta t, t + \delta t) = \mathbf{f}(\mathbf{r}, t) - Q^{-1} \Lambda_f (\mathbf{m}_f(\mathbf{r}, t) - \mathbf{m}_f^{\mathrm{eq}}(\mathbf{r}, t)) + \delta t \left(\mathbf{I} - \frac{1}{2} Q^{-1} \Lambda_f Q\right) \mathbf{G}(\mathbf{r}, t), \tag{10}$$

$$\mathbf{g}(\mathbf{r} + \mathbf{e}_i \delta t, t + \delta t) = \mathbf{g}(\mathbf{r}, t) - Q^{-1} \Lambda_g (\mathbf{m}_g(\mathbf{r}, t) - \mathbf{m}_g^{\mathrm{eq}}(\mathbf{r}, t)), \tag{11}$$

where $i = 1, 2, \ldots, N$, $\mathbf{f}$ and $\mathbf{g}$ are the respective vectors of the density and order-parameter distribution functions at lattice location $\mathbf{r}$ and time $\mathbf{t}$. $\Lambda_{\alpha(\alpha=f,g)}$ is the diagonal relaxation matrix give by

$$\Lambda_\alpha = \mathrm{diag}(s_{\alpha 0}, s_{\alpha 1}, \ldots, s_{\alpha N-1}), \tag{12}$$

and Q is a $N \times N$ matrix which linearly transforms the distribution functions $\mathbf{f}$ and $\mathbf{g}$ to the velocity moments $\mathbf{m}_f$ and $\mathbf{m}_g$, respectively with

$$\mathbf{m}_f = Q \cdot \mathbf{f}, \tag{13}$$

$$\mathbf{m}_g = Q \cdot \mathbf{g} \tag{14}$$

The body-face symbols $\mathbf{f}$, $\mathbf{g}$, $\mathbf{m}$ and $\mathbf{G}$ denote the dimensional column vectors and have

$$\mathbf{f}(\mathbf{r}, t) := (f_0, f_1, \ldots, f_{N-1})^{\mathrm{T}}, \qquad \mathbf{g}(\mathbf{r}, t) := (g_0, g_1, \ldots, g_{N-1})^{\mathrm{T}},$$

$$\mathbf{m}_f(\mathbf{r}, t) := (m_{f0}, m_{f1}, \ldots, m_{fN-1})^{\mathrm{T}},$$

$$\mathbf{m}_g(\mathbf{r}, t) := (m_{g0}, m_{g1}, \ldots, m_{gN-1})^{\mathrm{T}},$$

$$\mathbf{G}(\mathbf{r}, t) := (G_0, G_1, \ldots, G_{N-1})^{\mathrm{T}}.$$

Here T denotes the transpose operator, and $\mathbf{G}$ represents the body forcing, of which components are

$$\mathbf{G}_i = w_i \frac{(\mathbf{e}_i - \mathbf{u})}{c_s^2} \cdot (\mathbf{F}_b + \mu \nabla \varphi), \tag{15}$$

where $\mu\nabla\varphi$ comes from the pressure tensor (see Eq. (7)) and w_i is the weight coefficients dependent on the discrete velocity model. For the three-dimensional 19-discrete-velocity (D3Q19) model with $c_s = 1/\sqrt{3}(\delta r = \delta t = \delta = 1)$, the discrete velocities and weighting coefficients are

$$\mathbf{e}_i = \begin{cases} (0,0,0), & i = 0 \\ (\pm1,0,0),(0,\pm1,0),(0,0,\pm1), & i = 1-6 \\ (\pm1,\pm1,0),(\pm1,0,\pm1),(0,\pm1,\pm1), & i = 7-18 \end{cases};$$

$$w_i = \begin{cases} \dfrac{1}{3}, & i = 0 \\ \dfrac{1}{18}, & i = 1-6 \\ \dfrac{1}{36}, & i = 7-18 \end{cases}, \tag{16}$$

and the 19 equilibrium moments and their corresponding relaxation coefficients in Λ_α are given in Table 1.

It should be noted that all the nonlinear velocity terms can be omitted in the equilibria of $\{m_{gi}^{eq}\}$ because the fourth order isotropic lattice tensor is not required in recovering the Cahn–Hilliard equation (Eq. (6)) [32]. The relaxation parameters chosen in this work is followed the analysis of the MRT model [34] to reduce the viscosity-dependence velocity field. The transformation matrix Q for the D3Q19 model is given in [34].

The local density ρ, the order parameter φ and the momentum $\mathbf{j}$ are calculated, respectively as

$$\rho = \sum_i f_i, \tag{17}$$

$$\varphi = \sum_i g_i, \tag{18}$$

$$\mathbf{j}{:=}(j_x, j_y, j_z) = \sum_i f_i \mathbf{e}_i + \frac{\delta}{2}\rho_0 \mathbf{G}. \tag{19}$$

It should be indicated that the density ρ defined in our work can be thought as a nominal density, the real local density should be obtained in terms of the order parameter as $\rho(\varphi) = \rho_g + (\varphi - \varphi_g)(\rho_l - \rho_g)/(\varphi_l - \varphi_g)$, where φ_l and φ_g are the upper and lower limits of the order parameter and can be determined by the Maxwell's equal-area rule. The reason we use the nominal density in our work is that the value of it changes little in the whole flow field and thus the incompressible limit of the LBM is satisfied. On the other hand, the density difference is reflected in the order parameter φ and its related chemical potential μ, which acts as a force and is added in the flow field. The magnitude of this force is controlled by the surface tension and the interface thickness only. Therefore, large density difference cases can be handled easily and stability is not critical in this model. Besides this, one can note that all the elements in Q are integers and the inverse of the matrix Q can be calculated by $Q^{-1} = Q^T/(Q\cdot Q^T)$ because Q is an orthogonal matrix, therefore, the program can be efficiently coded by hand to reduce time-consuming matrix operations and thus enhancing computational efficiency in running the program. The main steps in the implementation of the present method can be summarized as the following:

- *Step 1*: Compute moments $\{m_{fi}^{eq}\}$ and $\{m_{gi}^{eq}\}$ from the fluid density and velocity (initially setting $m_{fi} = m_{fi}^{eq}$ and $m_{fi} = m_{fi}^{eq}$).

Table 1
Equilibrium moments and their corresponding relaxation coefficients of f and g (ρ_0 is the initial value of the density, $\tau_f = 3\eta/(\rho\delta t) + 0.5$ and $\tau_g = M/\Gamma + 0.5$ and Γ is a free parameter controlled the mobility)

$m_{f0}^{eq} = \rho$	$s_{f0} = 0$	$m_{g0}^{eq} = \varphi$	$s_{g0} = 0$
$m_{f1}^{eq} = -11\rho + 19\dfrac{\mu\varphi}{c_s^2} + 19\dfrac{\mathbf{j}\cdot\mathbf{j}}{\rho_0}$	$s_{f1} = \dfrac{1}{\tau_f}$	$m_{g1}^{eq} = -30\varphi + 19\dfrac{\Gamma\mu}{c_s^2}$	$s_{g1} = \dfrac{1}{\tau_g}$
$m_{f2}^{eq} = 3\rho - 9\dfrac{\mu\varphi}{c_s^2} - \dfrac{11}{2}\dfrac{\mathbf{j}\cdot\mathbf{j}}{\rho_0}$	$s_{f2} = s_{f1}$	$m_{g2}^{eq} = 12\varphi - 9\dfrac{\Gamma\mu}{c_s^2}$	$s_{g2} = s_{g1}$
$m_{f3,5,7}^{eq} = j_{x,y,z}$	$s_{f3,5,7} = 0$	$m_{g3,5,7}^{eq} = \dfrac{\varphi}{\rho_0} j_{x,y,z}$	$s_{g3,5,7} = 0$
$m_{f4,6,8}^{eq} = -\dfrac{2}{3} j_{x,y,z}$	$s_{f4,6,8} = 8\dfrac{(2 - s_{f1})}{(8 - s_{f1})}$	$m_{g4,6,8}^{eq} = -\dfrac{2\varphi}{3\rho_0} j_{x,y,z}$	$s_{g4,6,8} = 8\dfrac{(2 - s_{g1})}{(8 - s_{g1})}$
$m_{f9}^{eq} = \dfrac{3j_x^2 - \mathbf{j}\cdot\mathbf{j}}{\rho_0}$	$s_{f9} = s_{f1}$	$m_{g9}^{eq} = 0$	$s_{g9} = s_{g1}$
$m_{f10}^{eq} = -\dfrac{3j_x^2 - \mathbf{j}\cdot\mathbf{j}}{2\rho_0}$	$s_{f10} = s_{f1}$	$m_{g10}^{eq} = 0$	$s_{g10} = s_{g1}$
$m_{f11}^{eq} = \dfrac{j_y^2 - j_z^2}{\rho_0}$	$s_{f11} = s_{f1}$	$m_{g11}^{eq} = 0$	$s_{g11} = s_{g1}$
$m_{f12}^{eq} = -\dfrac{j_y^2 - j_z^2}{2\rho_0}$	$s_{f12} = s_{f1}$	$m_{g12}^{eq} = 0$	$s_{g12} = s_{g1}$
$m_{f13}^{eq} = \dfrac{j_x j_y}{\rho_0}$	$s_{f13} = s_{f1}$	$m_{g13}^{eq} = 0$	$s_{g13} = s_{g1}$
$m_{f14}^{eq} = \dfrac{j_y j_z}{\rho_0}$	$s_{f14} = s_{f1}$	$m_{g14}^{eq} = 0$	$s_{g14} = s_{g1}$
$m_{f15}^{eq} = \dfrac{j_x j_z}{\rho_0}$	$s_{f15} = s_{f1}$	$m_{g15}^{eq} = 0$	$s_{g15} = s_{g1}$
$m_{f16-18}^{eq} = 0$	$s_{f16-18} = s_{f1}$	$m_{g16-18}^{eq} = 0$	$s_{g16-18} = s_{g1}$

- *Step 2*: Calculation the equilibria $\{m_{fi}^{eq}\}$ and $\{m_{gi}^{eq}\}$ in the moment space.
- *Step 3*: Compute the post-collision density distribution functions by Eqs. (10) and (11).
- *Step 4*: Advecting the distribution function $\{f_i\}$ and $\{g_i\}$.

2.3. Boundary conditions and numerical evaluation of the derivatives

One of the advantages of the LB method over the conventional Navier–Stokes solvers is the implementation of the boundary condition on the complex geometries like the GDL structure shown in Fig. 1. Theoretically, this kind of geometry can only be approximated by the zigzag grids (see Fig. 2) due to the difficulties of experimental measuring or mathematical describing the exact boundary positions. In this situation, the standard bounce back boundary condition of the LB method provides an efficient and simple way to model the non-slip condition in terms of the distribution functions $\{f_i\}$. As shown in Fig. 2, the unknown distribution functions (black dash arrow) coming from the solid part can be simply set to the known values of their corresponding ones with opposite directions (blue solid arrow) and the actual non-slip boundary can be realized at the one-half grid spacing beyond the last fluid node [23].

Since the wetting boundary condition (Eq. (4)) is an equilibrium condition, it is appropriate to impose it through the equilibria $\{m_{gi}^{eq}\}$ [35]. From Eq. (4), to set the equilibrium boundary condition we usually need to calculate the normal vector of the boundary so that the order parameter φ and its second derivatives $\nabla^2\varphi$ on the boundary nodes are obtained. However, as we stressed earlier, it is difficult for the geometries like the GDL. To avoid this difficulty, in this work we use an approximation strategy to evaluate them. In Fig. 2, the boundary point P (red solid circle) is surrounded by some fluid points (blue solid circle) and some solid points (black solid circle). To obtain the values of φ and $\nabla^2\varphi$ on the point P, Taylor series expansions of φ on the nearest and next-nearest neighboring fluid-side points of the point P (see Fig. 2) are carried out, and for each expansion point we have $\varphi_P = \varphi_{f,l} - \delta\partial_r\varphi + O(\delta^2)$, which can be further approximated by $\varphi_P \cong \varphi_{f,l} - \delta\partial_n\varphi$. Therefore, on average, the order

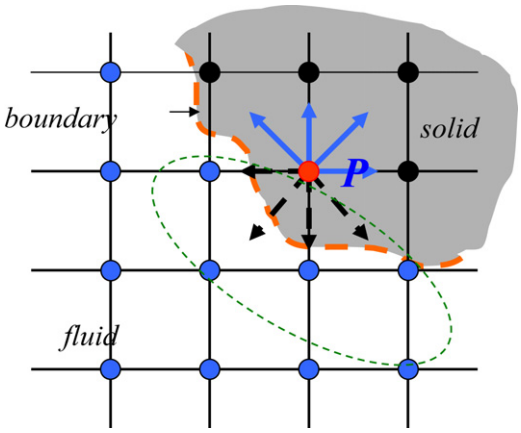

Fig. 2. 2D sketch of implementations of the boundary conditions of complex geometry (fluid points: blue solid circle; solid points: black solid circle; the nearest and next-nearest fluid-side points: inside the green dash elliptic circle).

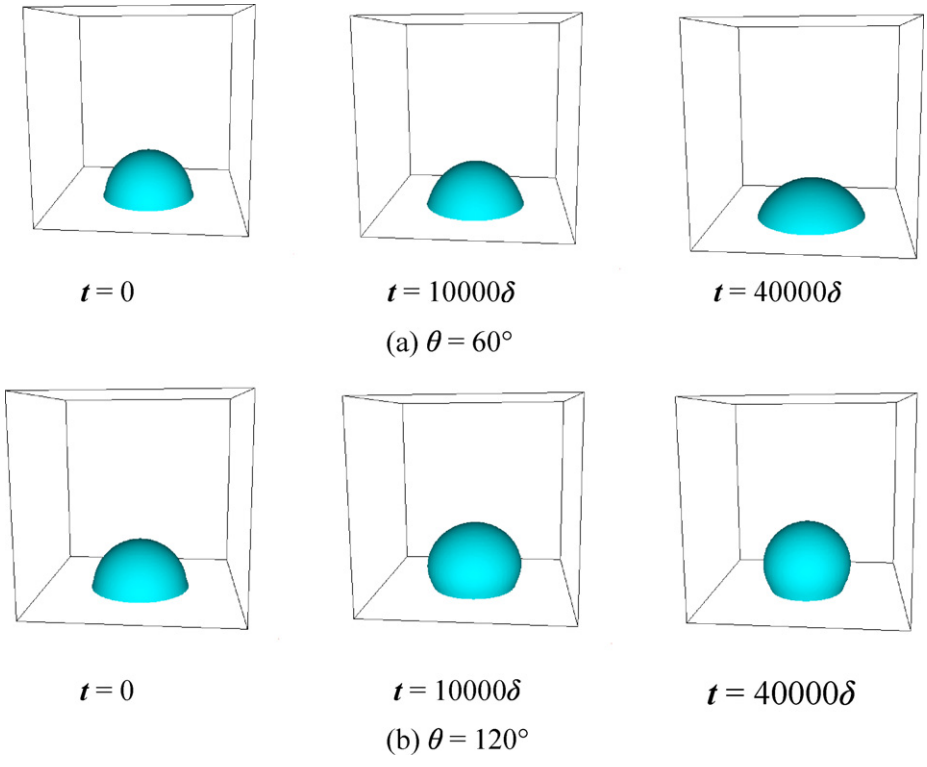

Fig. 3. Time variations of the spreading and shrinking droplet shape at $\theta = 60°$ and 120°, respectively. The isosurface represents the order parameter $\varphi = 0$.

parameter φ and its second derivatives $\nabla^2\varphi$ on the point P can be approximated as:

$$\varphi_P \cong \frac{\sum_l(\varphi_{f,1} - \delta\partial_n\varphi_P)}{N} = \frac{\sum_l(\varphi_{f,1} + |\delta|(\gamma/k))}{N}, \quad (20)$$

$$\nabla^2\varphi_P \cong \frac{2\sum_l(\varphi_{f,1} - \varphi_P - \delta\partial_n\varphi_P)}{N} = \frac{2\sum_l(\varphi_{f,1} - \varphi_P + |\delta|(\gamma/k))}{N}, \quad (21)$$

where δ is the unit grid space and $\varphi_{f,l}$ is the order parameters on the nearest and next-nearest neighboring fluid-side points of the point B; $l = 1, 2, \ldots, N$ with N representing the total number of the nearest and next-nearest fluid-side points of the point P; γ can be calculated from Eq. (4) directly. The implementation of Eqs. (20) and (21) is straightforward by using the lattice stencils, and one can judge and count the fluid-side points by the streaming directions of the discrete velocities whether pointing to fluid field or not.

In the LB framework, the first order and second order derivatives of φ in the fluid field can also be conventionally calculated by using the lattice stencils so that the discretization errors are reduced. In this work, the following stencil scheme is used:

$$\nabla_j\varphi = \frac{3\sum_i w_i\varphi(\mathbf{r} + \mathbf{e}_i\delta t, t + \delta t)e_{ij}}{\delta t}, \quad (22)$$

$$\nabla^2\varphi = \frac{-24\varphi(\mathbf{r}, t) + 36\sum_i w_i\varphi(\mathbf{r} + \mathbf{e}_i\delta t, t + \delta t)}{6(\delta t)^2}, \quad (23)$$

where $j = 1, 2, 3$ denotes the dimensions.

3. Results and discussion

3.1. Model validation

To validate the present model, a static droplet held on a wall is simulated, and the contact angle is tested. A hemispheric droplet with radius R placed on a wall is considered and it is brought to the equilibrium state at rest under the effects of the wetting potential γ imposed on wall. The computational domain is divided into a $51 \times 51 \times 51$ cubic lattice with $\delta = 1$ and its edges parallel to the x, y and z coordinate axes. The radius of the droplet R is set 10δ or 15δ. The other parameters used are $\rho_l/\rho_g = 1000$, $\eta_l/\eta_g = 100$, $\rho_g = 1$, $\eta_g = 0.1$, $\sigma = 7.86 \times 10^{-2}$, $\xi = 4.5\delta$ and $\Gamma = 10^{-2}$. The contact angle is changed in the range

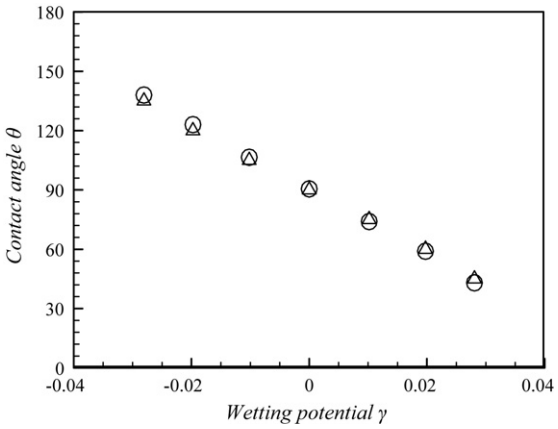

Fig. 4. Comparison of calculated contact angles with the theoretical predictions (Eq. (4)) (triangle, theoretical prediction; circle, simulation results).

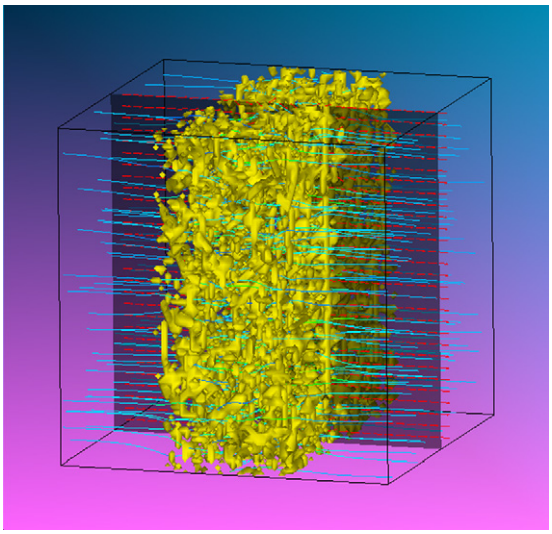

Fig. 5. A model of 3D gas-diffusion-layer with edges parallel to the main flow directing from left to right. Slice shows the velocity vectors at a mid-plane parallel to the main flow direction ($\delta p = 1.7 \times 10^{-3}$, $\theta = 120°$, $\eta_l/\eta_g = 100$).

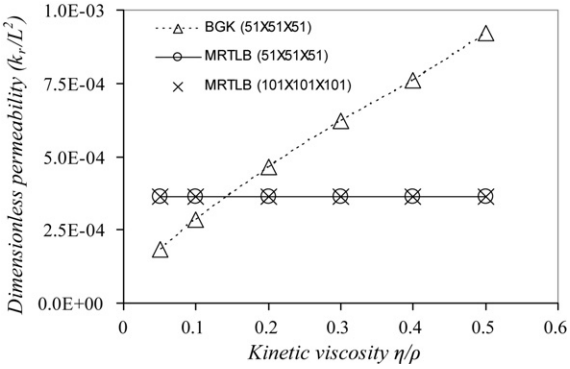

Fig. 6. Comparison of the calculated absolute permeability of the GDL as a function of the fluid kinetic viscosity.

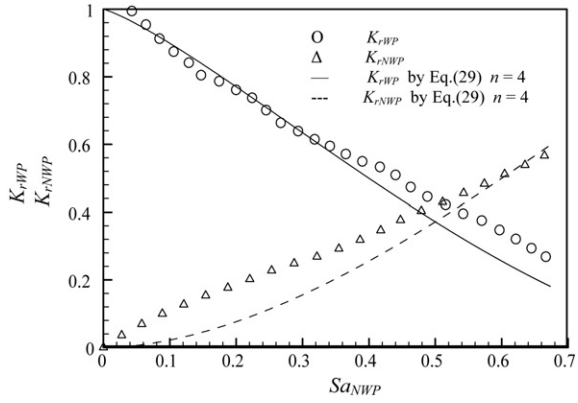

Fig. 7. Comparison of the relative permeabilities obtained by the present model and van Genuchten function (Eq. (29)).

of $45^\circ \leq \theta \leq 145^\circ$. Periodic boundary conditions are applied in both x and y directions and non-slip/wetting boundary conditions are used at top and bottom walls in z direction. For this problem, the equilibrium radius R_c and contact angle θ_c of the droplet can be calculated by the following formula [36]:

$$R_c = \frac{1}{2}\left(h + \frac{b^2}{4h}\right), \tag{24}$$

$$\theta_c = \arctan\left(\frac{b}{2(R-h)}\right), \tag{25}$$

where h is the height of the droplet and b is the contact length of the droplet connecting to the wall.

Fig. 3(a) and (b) shows the time variations of the droplet on the hydrophilic ($\theta = 60^\circ$) and hydrophobic ($\theta = 120^\circ$) walls, respectively. It is seen from Fig. 3(a), the droplet spreads as the time passes and finally reaches to its equilibrium shape with the calculated contact angle $\theta_c = 59^\circ$. As shown in Fig. 3(b), the connecting area between the droplet and the wall reduces as the time passes, and the droplet reaches its equilibrium shape with $\theta_c = 122^\circ$. Fig. 4 shows the variation of the calculated contact angle with the wetting potential γ. The present results are in good agreement with the theoretical curve obtained by Eq. (4). The

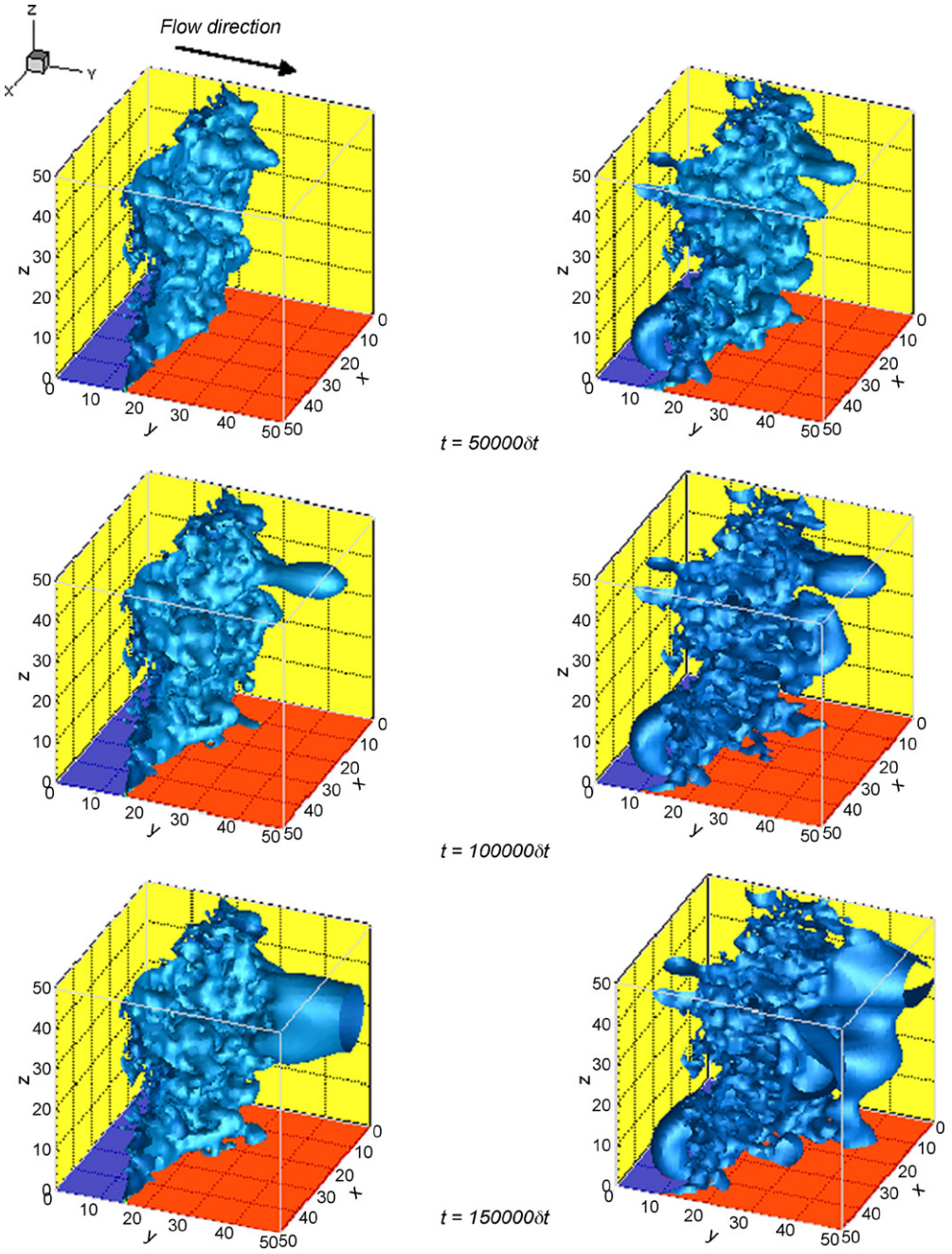

Fig. 8. Snapshots of the liquid-gas transport processes in the model of GDL at $\delta p = 1.7 \times 10^{-3}$ (left row) and 3.4×10^{-3} (right row), respectively. Flow direction is indicated by the arrow on the top of the figure.

agreement between the theory and our simulation indicates that the present method handles the two-phase flows with wetting boundaries correctly.

3.2. Liquid-gas flows in GDL

For the works presented in this section, we fit a 3D-geometry to a carbon-fiber structure of the GDL with a porosity of 80.3% and characteristic pore scale 10 μm (see Fig. 1) by the DPD method [37]. The carbon fiber made in the GDL is hydrophobic, and therefore in the following the gas phase is denoted as the wetting phase (WP) while the liquid phase as non-wetting phase (NWP) for brevity. The computational domain is discretized by $51 \times 51 \times 51$ or $101 \times 101 \times 101$ cubic lattice with the same coordinate arrangement as in the case of Section 3.1. Periodic boundary conditions are used on all sides of the domain for the velocity field. For the order parameter, it is assumed to be equal to 1 (liquid phase) at one side and −1 (gas phase) at the opposite side and the other four sides are treated as periodic boundaries. Unless otherwise indicated, other parameters used in the simulations of this section are same as those used in Section 3.1.

3.2.1. Absolute permeability and comparison between the BGK and MRT model

The mathematical basis of immiscible two-phase flows in a porous medium is Darcy's law, written as

$$\bar{\mathbf{u}} = -\frac{\mathbf{K}(k_{ij})}{\eta}\nabla p, \tag{26}$$

where $\bar{\mathbf{u}}$ denotes the average flow velocity and $\mathbf{K}$ represents the absolute permeability tensor of the porous medium. The component k_{ij} of the permeability tensors represents the permeability of the material in the direction parallel to the jth coordinate axis if the main flow direction is parallel to the ith coordinate axis. For convenience, here we assume that the edges of the sample are parallel to the Cartesian coordinate axes. As a direct consequence, the off-diagonal elements of $\mathbf{K}$ are equal to zero. Furthermore, if the pressure gradient (i.e., the main flow direction) is parallel to the ith coordinate axis, Darcy's law reduces to the scalar equation and we have

$$k_{ii} = -\frac{\eta L \bar{u}_i}{\delta p}, \tag{27}$$

where $\bar{u}_i$ is the average flow speed, L the length of the medium edge which is parallel to the ith coordinate axis, and δp stands for the pressure difference across the medium in the ith direction. The present situation is visualized in Fig. 5, which shows streamlines of the velocity field at $\delta p = 1.7 \times 10^{-3}$, $\theta = 120^\circ$ and $\eta_l/\eta_g = 100$.

The absolute permeability of the GDL with respect to different fluid kinetic viscosities is also calculated. In this simulation, a constant pressure drop $\delta p = 1.7 \times 10^{-3}$ is applied to the single-phase flow through the GDL on the $51 \times 51 \times 51$ and $101 \times 101 \times 101$ grids. To show the advantage of the MRT model over its BGK counterparts, the simulation using the BGK model is carried out at the same time. Fig. 6 shows the calculated absolute permeabilities at various viscosities obtained by the MRT and BGK models. It is clearly seen that the permeabilities obtained by the MRT model remain essentially constant for both grid sets when the viscosity changes. However, the results of the BGK simulation change significantly and increase with increasing viscosity. Therefore, compared to the BGK model, the present MRT model is more suitable for simulating multiphase flow systems, in which different viscosities coexist. In addition, by using the MRT model for the multiphase flow systems, computational efficiency can be enhanced by using coarser grid set while desired accuracy is achieved. Based on the above observations, all the following simulations use the $51 \times 51 \times 51$ grid set.

3.2.2. Relative permeability and effects of pressure drop, wettability and viscosity ratio

The relative permeability $\mathbf{K}_r$ is defined by an extension of Darcy's law to

$$\bar{\mathbf{u}} = -\frac{\mathbf{K}_r(\mathrm{Sa})\mathbf{K}}{\eta}\nabla p, \tag{28}$$

where Sa (ratio of phase volume over pore volume in GDL) reflects that the permeability depends on the saturation. Using Eq. (28) we can calculate $\mathbf{K}_r(\mathrm{Sa})$ for both wetting and non-wetting phases. Theoretically, the relative permeabilities can be written in terms of the saturations of each phase as the well known van Genuchten function

$$\mathbf{K}_r(\mathrm{Sa}) = \mathrm{Sa}^{1/3}(1 - (1 - \mathrm{Sa})^{(n-1)/n})^{2(n-1)/n} \tag{29}$$

where the values of n are in the range of $2 \le n \le 5$. Fig. 7 shows the comparison of the calculated $\mathbf{K}_r(\mathrm{Sa})$ by the present model and Eq. (29). Seen from this figure, the results obtained by the present model generally agree with the solutions of Eq. (29). With the increase of the NWP saturation, and the WP permeability decreases while the NWP permeability increases. In order to make a deep insight of the relative permeability, in the following we first investigate the dependency of the relative permeability on the pressure drop δp. In this case, we fix the contact angle $\theta = 120^\circ$ and viscosity ratio $\eta_l/\eta_g = 100$, and examine the effects of two values of pressure drop $\delta p = 1.7 \times 10^{-3}$ and 3.4×10^{-3}, respectively.

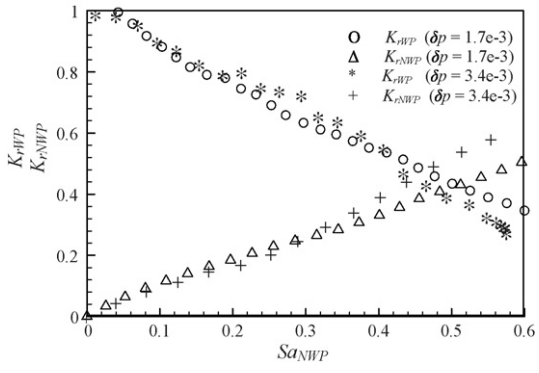

Fig. 9. Relative permeability vs. NWP saturation for liquid-gas flow in GDL at different δp with $\theta = 120^\circ$.

Fig. 8 shows snapshots of the liquid-gas transport processes in the GDL at three different time steps at $\delta p = 1.7 \times 10^{-3}$ and 3.4×10^{-3}, respectively. For clearly displaying the liquid transportation, the GDL structure is not shown in this figure and the following Fig. 11. As illustrated in Fig. 8, larger δp drives the NWP to move faster than the small δp because larger driving force more easily overcomes the capillary resistance due to the interface tension. The influence of δp on the relative permeability $\mathbf{K}_r$ for both NWP and WP is shown in Fig. 10. As shown in Fig. 9, when δp is increased, the WP relative permeability does not change much for the range of the NWP saturation. However, the NWP permeability is increased slightly at the intermediate NWP saturation. These observations are in agreement with previous numerical and experimental works [22,36].

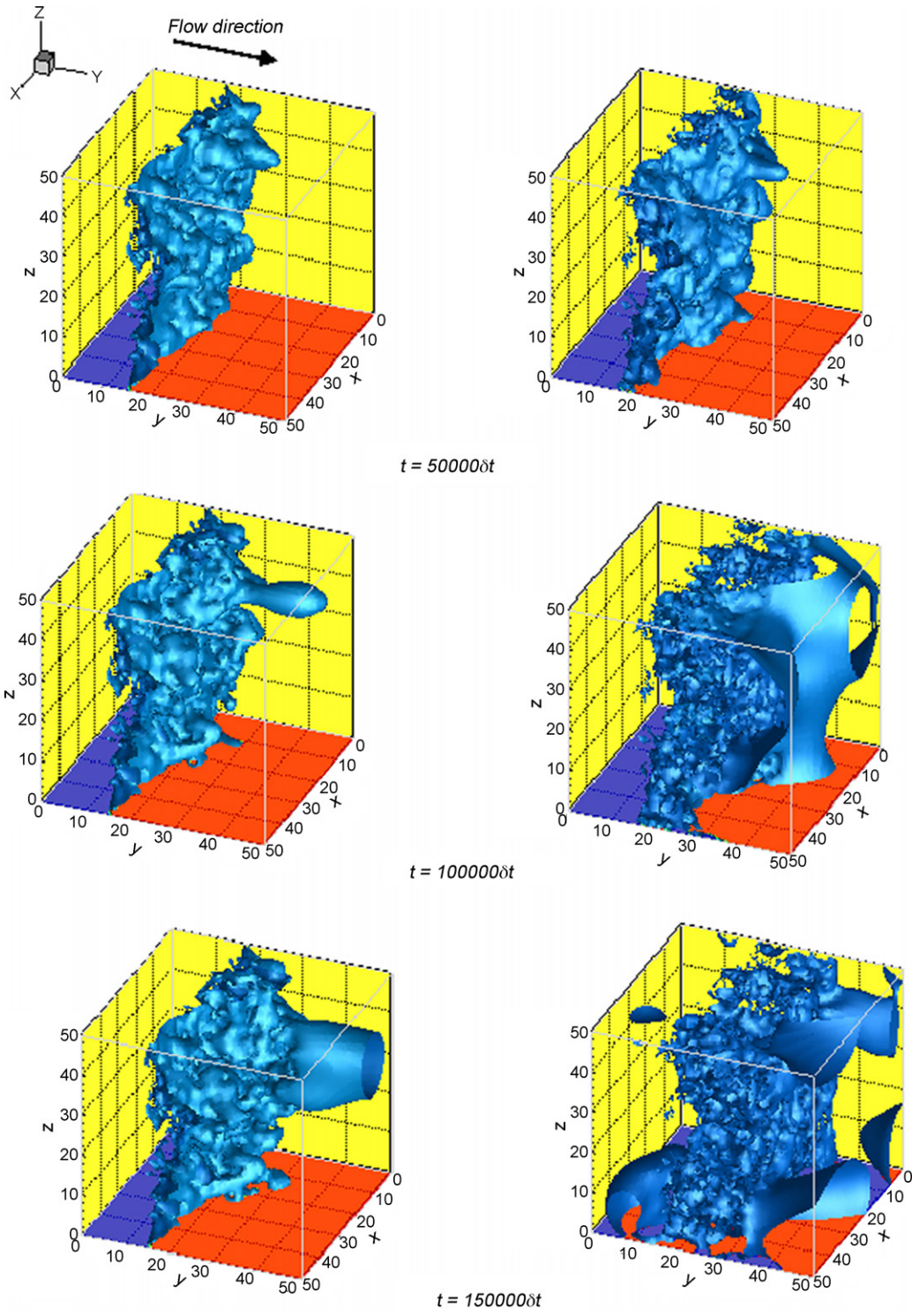

Fig. 10. Snapshots of the liquid-gas transport processes in the model of GDL at contact angles $\theta = 105^\circ$ (left row) and 120° (right row), respectively. Flow direction is indicated by the arrow on the top of the figure.

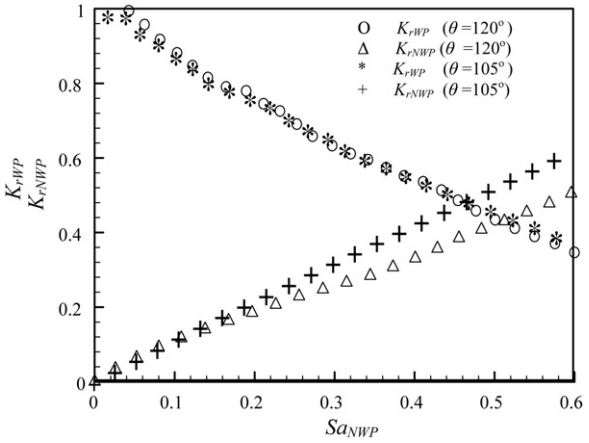

Fig. 11. Relative permeability vs. NWP saturation for liquid-gas flow in GDL at different contact angles with $\delta p = 1.7 \times 10^{-3}$ and $\eta_l/\eta_g = 100$.

Next, the effects of the wettability on the relative permeabilities at $\delta p = 1.7 \times 10^{-3}$ and $\eta_l/\eta_g = 100$ are studied. The wettability of the wall is controlled by tuning the contact angle θ. Here, two contact angles $\theta = 105^\circ$ and 120° are examined. Fig. 10 shows snapshots of the liquid-gas transport processes with the two contact angles in the GDL at three different time steps. As illustrated in this figure, at the smaller contact angle $\theta = 105^\circ$, i.e. a stronger wettability of the GDL, the NWP transport faster than that at $\theta = 120^\circ$. The reason behind this phenomenon is obvious: the stronger the wettability of the GDL has, the larger the driven force imposed on the liquid, and hence the easier the liquid movement overcomes the resistance of the capillary force. This mechanism also leads to a higher NWP relative permeability in the strong-wettability GDL than in the weak-wettability one, and this finding can be observed in Fig. 11, which shows $\mathbf{K}_r$ for both NWP and WP as a function of the NWP saturation at contact angles $\theta = 105^\circ$ and 120°, respectively. Again, the observations from Figs. 10 and 11 are in agreement with previous numerical and experimental works [22,36].

The viscosity-ratio effects on the relative permeability at $\delta p = 1.7 \times 10^{-3}$ and $\theta = 120^\circ$ are further studied in Fig. 12, which shows the relative permeabilities of the NWP and WP as a function of the NWP saturation for two viscosity ratios, $\eta_l/\eta_g = 10$ and $\eta_l/\eta_g = 100$. Consistent with the findings in the previous works [22,36], we also observe that a decreased relative permeability of the NWP is caused by an increased viscosity ratio, especially at intermediate saturation. This phenomenon can be attributed to the so-called "lubricating" effect on the liquid flow due to a gas film, which is caused by that, gas flowing in relatively small pores is strongly coupled to the liquid flowing in the larger regions of pore structure, and makes liquid experience an apparent hydraulic slip [36]. The greater the viscosity ratio, the greater the hydraulic slip becomes. On the other hand, as shown in Fig. 12, the relative permeability of the WP slightly increases, which indicates that the lubricating effect cause an increase of the WP average velocity and hence the WP relative permeability.

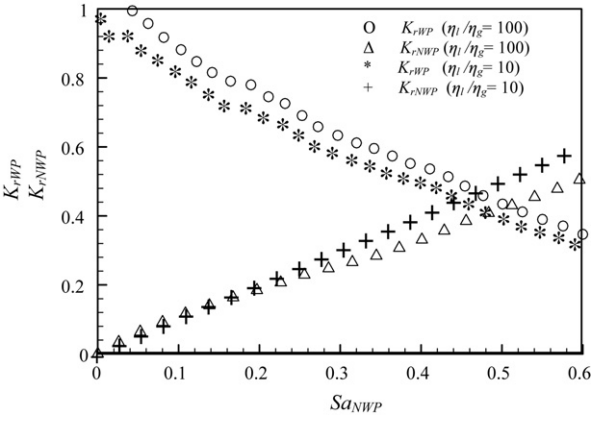

Fig. 12. Relative permeability vs. NWP saturation for liquid-gas flow in GDL at different viscosity ratios with $\delta p = 1.7 \times 10^{-3}$ and $\theta = 120^\circ$.

4. Conclusions

In this paper, a MRTLB model is presented and applied to simulate water-gas transportations in the GDL of a PEM fuel cell. The model is based on the diffuse interface theory, and employs two distributions so that multiphase flows with large density ratios and various viscosities can be handled. The interface tension and wetting boundary condition in the present model are straightforwardly implemented. To numerically realize the boundary conditions for the complicated structure like GDL, besides the standard bounce back condition used for the non-slip condition, an approximated average scheme based on the extrapolation method is derived to mimic wetting boundaries. The numerical validation of the static droplet on a wetting wall shows good agreement with the theoretical predictions. Compared to the conventional macroscopic multiphase models like volume-averaged or pore-level models, which cannot track the interface itself, the present MRTLB model tracks the phase interface automatically and has advantages in programming simplicity, intrinsic parallelism and straightforward resolution of complex boundaries. Furthermore, the present model can easily handle the three-dimensional cases as shown in this paper.

The water-gas transportation in a 3D modeled GDL structure is simulated and the transport properties including absolute and relative permeabilities are calculated. The effects of the pressure drop, wettability and viscosity ratio on the relative permeability are also investigated. The obtained results show the expected trend as in the previous numerical and experimental works. This investigation demonstrates that the present multiphase MRTLB model is potentially a viable method for the flows in fuel cells.

Acknowledgements

The authors express their appreciation to Dr. S. Yamamoto of Toyota Central R&D Labs. for generating the 3D structure data of the GDL, and to Professors Yong Tian Chew and Chang Shu of University of Singapore for their inspiring suggestions on the method. A part of this work was supported by Core Research for Evolutional Science and Technology (CREST) of Japan Science and Technology (JST) Agency (No: 228205R) and the Japan

Society for the Promotion of Science through a Grant-in-Aid for Scientific Research (B) (No. 18360050).

References

[1] M. Mathias, J. Roth, J. Fleming, W. Lehnert, Handbook of Fuel Cells—Fundamentals, Technology and Applications, 2003, pp. 1–21 (Chapter 46).
[2] C. Manwart, R. Hilfer, Phys. Rev. E 59 (1999) 5596.
[3] T.E. Springer, T.A.Z. Awodzinski, S. Gottesfeld, J. Electrochem. Soc. 138 (1991) 2334.
[4] S. Um, C.Y. Wang, K.S. Chen, J. Electrochem. Soc. 147 (2000) 4485.
[5] S. Um, C.Y. Wang, J. Power Sources 125 (2004) 40.
[6] U. Pasaogullari, C.Y. Wang, Electrochim. Acta 49 (2004) 4359.
[7] U. Pasaogullari, C.Y. Wang, J. Electrochem. Soc. 151 (2004) A399.
[8] C.Y. Wang, Chem. Rev. (2004) 4727.
[9] M.H. Chang, F. Chen, H.S. Teng, J. Power Sources 160 (2006) 268.
[10] G. He, P. Ming, Z. Zhao, A. Abudula, Y. Xiao, J. Power Sources 163 (2007) 864.
[11] L. Pisani, M. Valentini, G. Murgia, J. Electrochem. Soc. 150 (2003) A1558.
[12] G.Q. Wang, C.Y. Wang, Presented at the 204th Electrochemical Society Meeting on Direct Numerical Simulation of PEM Fuel Cell Electrodes on the Pore Level, Orlando, FL, October, 2003.
[13] T.E. Springer, T.A. Zawodinski, S. Gottesfeld, in: R.E. White, M.W. Verbrugge, J.F. Stockel (Eds.), Modeling of Batteries and Fuel Cells, vol. 91–10, Softbound Proceedings Series, The Electro-chemical Society, Pennington, NJ, 1991, p. 209.
[14] M.L. Perry, J. Newman, E.J. Cairns, J. Electrochem. Soc. 145 (1) (1998) 5.
[15] M. Eikerling, A.A. Kornyshev, J. Electroanal. Chem. 453 (1998) 89.
[16] P. Quan, M.C. Lai, J. Power Sources 164 (2007) 222.
[17] D.H. Rothman, J.M. Keller, J. Stat. Phys. 52 (1988) 1119.
[18] X. Shan, H. Chen, Phys. Rev. E 47 (3) (1993) 1815.
[19] M.R. Swift, W.R. Osborn, J.M. Yeomans, Phys. Rev. Lett. 75 (1995) 830.
[20] X. He, S. Chen, R. Zhang, J. Comput. Phys. 152 (2) (1999) 642.
[21] T. Inamuro, T. Ogata, S. Tajima, N. Konishi, J. Comput. Phys. 198 (2004) 628.
[22] H. Li, C. Pan, C.T. Miller, Phys. Rev. E 72 (2005) 026705.
[23] C. Pan, L.-S. Luo, C.T. Miller, Comput. Fluids 35 (2006) 898.
[24] U. Frisch, B. Hasslacher, Y. Pomeau, Phys. Rev. Lett. 56 (1986) 1507.
[25] U. Frisch, D. d'Humières, B. Hasslacher, P. Lallemand, Y. Pomeau, Complex Syst. 1 (1987) 649.
[26] H. Chen, S. Chen, W.H. Matthaeus, Phys. Rev. A 45 (1992) 5539.
[27] Y.H. Qian, D. d'Humières, P. Lallemand, Europhys. Lett. 17 (1992) 479.
[28] P. Lallemand, L.-S. Luo, Phys. Rev. E 68 (2003) 066614.
[29] M.E. McCracken, J. Abraham, Phys. Rev. E 71 (2005) 036701.
[30] D. Jacqmin, J. Comput. Phys. 155 (1999) 96–127.
[31] V.M. Kendon, M.E. Cates, I. Pagonabarraga, J.C. Desplat, P. Bladon, J. Fluid Mech. 440 (2001) 147.
[32] H.W. Zheng, C. Shu, Y.T. Chew, Phys. Rev. E 72 (2005) 056705.
[33] J.W. Cahn, J. Chem. Phys. 66 (1977) 3667.
[34] D. d'Humières, I. Ginzburg, M. Krafczyk, P. Lallemand, L.-S. Luo, Philos. Trans. R. Soc. London A 360 (2002) 437.
[35] A.J. Briant, P. Papatzacos, J.M. Yeomans, Philos. Trans. R. Soc. London A 360 (2002) 485.
[36] F.A.L. Dullien, Porous Media: Fluid Transport and Pore Structure, Academic, San Diego, 1992.
[37] S. Yamamoto, Computational Phys. Lab., Toyota Central R&D Labs., Inc., private communication.